COMPARATIVE ANALYSIS OF PERFORMANCES OF DIFFERENT MOTOR-PROPELLER COMBINATIONS FOR THE CHARACTERIZATION OF ELECTRIC MOTORS EFFICIENCY

Mario Navarro-Zea, Sergio Esteban
Departamento de Ingeniería Aeroespacial y Mecánica de Fluidos
Universidad de Sevilla
Seville, Spain

ABSTRACT

This article presents a comprehensive characterization of electric propulsion systems, focusing on the performance of electric motors and propellers through wind tunnel experimentation. The study aims to deepen the understanding of the interrelation between key parameters—such as rotational speed (RPM) and incident airspeed—and their influence on overall system efficiency. The experimental setup, which integrates a continuous power supply and robust data acquisition methodology, enables precise and repeatable measurements. By conducting a wide range of tests under varying conditions, the research not only yields valuable insights into motor and propeller behavior but also establishes a solid foundation for the development of accurate multi-variable models. These models are essential for enhancing electric aircraft design, enabling improvements in autonomy, payload capacity, and operational range. Furthermore, the data generated can be directly integrated into existing flight simulators, providing a realistic basis for the performance prediction of electric aircraft. The methodology relies on the integration of a commercial test stand and software suite, enabling accessible and repeatable experimentation for the broader research community.

INTRODUCTION

The propulsive system is essential in the design, operation, and control of small electric aircraft. Proper functioning and integration of the propulsion components directly affect the aircraft's performance. This, in turn, has an immediate impact on range and endurance. Specifically, the motor-propeller combination is crucial and the best choice can vary depending on the operating regime.

This study is part of the ProVANT-EMERGENTIa project (*DevElopment of an unManned convERtible aircraft for rapid and efficient deployment in emenGENcy situaTIons*), which focuses on the design of a fixed-wing convertible RPAS with VTOL capabilities, intended for use in search-and-rescue (SAR) missions (Ref. 1). To validate the UAV's performance, accurate propulsion models are needed for integration into flight simulators.

Most wind tunnel experiments in the literature focus on propeller characterization, often neglecting the influence of the motor (Ref. 2) (Ref. 3). Additionally, CFD simulations—while powerful—are computationally intensive (Ref. 4), and Blade Element Momentum Theory (BEMT) models (Ref. 5), require reliable aerodynamic data to ensure accuracy. Within the scope of the ProVANT-EMERGENTIa project, initial data collection setups were developed, but the process was time-consuming and labor-intensive. The later integration of the *Tyto Robotics* test stand greatly simplified experimentation; however, reliance on batteries remained a significant limitation. This paper contributes an efficient testing methodology for electric propulsion systems, enabling precise and repeatable data collection. It defines optimal experimental procedures for identifying component performance limits and applies improved data processing techniques, enhancing the overall reliability and efficiency of aerodynamic testing in this field. The challenge is addressed through an analysis of configurations and carried out using the Series 1585 Test Stand provided by *Tyto Robotics* (Ref. 6), mounted in the wind tunnel from *Escuela Técnica Superior de Ingeniería*, Seville.

The structure of the work is as it follows. Firstly, a description of the experimental setup and its integration into the wind tunnel is done. Next, it follows with the description of the theoretical framework of the project, data processing methodology and the strategy used in the conducted test campaigns. The next section includes the analysis and comparison of the results obtained and, finally, some conclusions and future project lines are presented.

Copyright Statement
The authors confirm that they, and/or their company or organization, hold copyright on all of the original material included in this paper. The authors also confirm that they have obtained permission, from the copyright holder of any third-party material included in this paper, to publish it as part of their paper. The authors confirm that they give permission, or have obtained permission from the copyright holder of this paper, for the publication and distribution of this paper as part of the ERF proceedings or as individual offprints from the proceedings and for inclusion in a freely accessible web-based repository.

EXPERIMENTAL SETUP DESCRIPTION

In this section, a brief description of the experimental setup is provided. The selection and characteristics of the components, including motors, propellers, ESC, the test stand and its integration into the wind tunnel are discussed.

RCbenchmark's Test Stand: Series 1585

The RCbenchmark's Test Stand (Figure 1), manufactured by *Tyto Robotics* (Ref. 6), marks a significant advancement in the characterization of electric propulsion systems, offering the capability to collect and store a diverse range of data in a single, compact, and precise file. This feature greatly enhances the testing experience and facilitates result analysis. Its main characteristics are summarized in Table 1.

Table 1. Series 1585 Test Stand Characteristics.

Characteristic	Range	Tolerance	Unit
Thrust	-5 to 5	0.5% ± 0.001	kgf
Torque	-2 to 2	0.5% ± 0.001	Nm
Voltage	0 to 50	0.5%	V
Current	0 to 55	1%	A
Burst current	0 to 60	-	A
Angular speed[a]	0 to 190k	1	eRPM
Coil resistance	0.003 to 240	0.5%	Ohm

[a]Electrical RPM, divide by the number of motor poles to obtain true mechanical RPM.

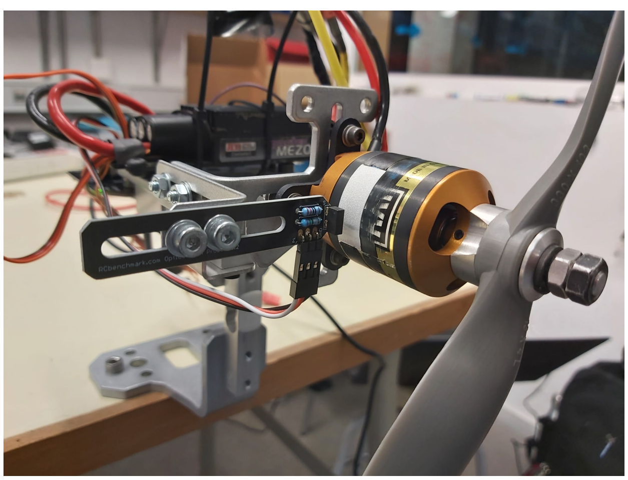

Figure 1. Series 1585 Test Stand.

Developed specifically to improve the efficiency of propulsion systems, it proves to be instrumental in the experimental setup. The test stand connects to a computer via USB and is operated using dedicated software, which enables real-time monitoring of both motor and propeller parameters throughout the tests. Noteworthy features include the versatile "Setup & Utilities" tab for unit selection, directory configuration, and firmware updates, alongside the "Safety Cutoffs" for establishing safety limits. The "Manual Control" section enables manual motor speed adjustments, while the "Automatic Control" feature simplifies tests and ensures repeatability. The software encompasses various programs, such as discrete and continuous sweeps, custom step sequences, and a UDP connection option. The calibration process is also conducted using the RCbenchmark software, employing a straightforward procedure. This allows calibration for thrust, weight and torque measurements, using a known load system. It is recommended to re calibrate the system if it has been disassembled, connections have been modified, or every two months to ensure the accuracy of the measurements.

BLDC Motors

The characterization is addressed to Brushless DC (BLDC) motors, a key component in small electric aircraft propulsion systems. BLDC motors offer significant advantages, combining high efficiency, precise control, and reduced maintenance compared to traditional brushed motors. They eliminate the need for brushes, minimizing wear and increasing longevity. Five motors have been characterized, sourced from two different manufacturers: Model Motors and Turnigy.

Model Motors, a key player in electric motor development, introduces the AXI series (Ref. 7), marking progress in brushless motor technology. Known for quality materials and ongoing improvement, both AXI 2826/10 (Figures 2, 3) and AXI 4130/16 (Figures 4, 5) have been tested. The first one is the smallest one, celebrated for its excellent power-to-weight ratio, while the second one is a larger motor representing advancements. Starting with the older versions, and then taking the leap to the enhanced V2 for both motors, that promise better cooling and material quality, consequently improving its efficiency. Meanwhile, Turnigy, known for electric components, steps in with the Aerodrive SK3 5045 (Figure 6). Positioned as an efficient and high-caliber motor, it adds diversity to the project.

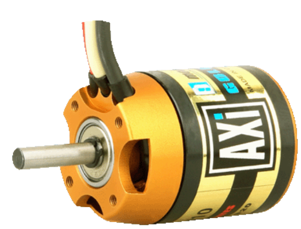

Figure 2. AXI 2826/10 V1.

Figure 3. AXI 2826/10 V2.

Electronic Speed Controller

The Electronic Speed Controller (ESC) regulates the electric motor by providing electrical signals translated into speed changes. BLDC motor controllers transform direct current from the source into three-phase alternating current. The ESC used in this project is the Mezon 115 Opto (Figure 7), developed by the company Jeti Model (Ref. 8). The Opto version does not include an integrated Battery Eliminator Circuit (BEC), so an additional power source is required to operate the servo and receiver.

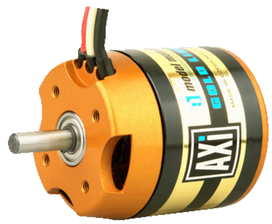

Figure 4. AXI 4130/16 V1.

Figure 5. AXI 4130/16 V2.

Figure 6. Aerodrive SK3 5045.

Figure 7. Mezon 115 Opto.

Propellers

The propellers used in the project belong to APC Propellers (Ref. 9), a company with extensive experience and a long-standing presence in the industry. Currently offering a range of over 500 propellers with diameters ranging from 4 to 27 inches, APC Propellers manufactures their propellers using composite materials, combining fiberglass and carbon fibers with nylon matrices. Their complete propeller catalog, categorized by different types, can be found on their website.

In the project's context, it is crucial to have a propeller selection with significantly different pitches to compare efficiency under various loads. Therefore, aligning with the chosen motors, the following *Thin Electric* category propellers are selected: 13x4E, 13x10E & 14x10E.

Propellers were selected to examine how variations in pitch and diameter influence system efficiency. The set includes two propellers with the same diameter but different pitch, and two with the same pitch but different diameter, enabling a structured comparison. Balancing the propellers is essential to prevent any undesirable vibrations during tests that could distort results and compromise safety. After positioning the propellers as shown in Figure 8, balance is achieved by removing material from the side that weighs more, ensuring optimal performance.

Power Supply

After considering its advantages, the decision was made to purchase the *eFuel 1200W* (Figure 9) power supply from the company *SkyRC* (Ref. 10). This unit converts the 100-240 V AC from the electrical grid to an output ranging from 15-30 V DC, with the capability of delivering up to 50 A of continuous power. This advancement over traditional LiPo batteries primarily offers two improvements: completely eliminating the dependence on charge cycles to conduct tests and allowing the realization of experiments with higher power and duration.

Figure 8. Propeller balancing.

Figure 9. *eFuel 1200W* power supply.

ETSI Wind Tunnel

This section describes the wind tunnel of the Aerospace Engineering and Fluid Mechanics Department at the *Escuela Técnica Superior de Ingeniería (Universidad de Sevilla)*, in which the propulsive experiments have been carried out. The mentioned tunnel is an open circuit one with closed cross-section and operates in a subsonic test speed regime. It consists mainly of 3 parts: a contraction chamber, a testing chamber and a diffuser (Figure 10). The testing chamber is the area where the studied element is located and has a length of 5 m and a rectangular cross-section of 1.4×1.8 m.

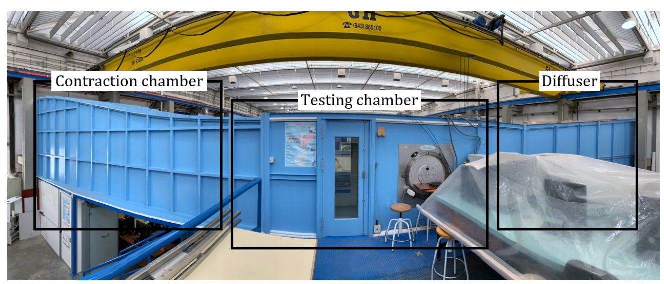

Figure 10. Panoramic view of the wind tunnel.

The maximum airspeed that the wind tunnel can achieve is 30 m/s. The fluid is accelerated by nine fans (HCT-90-4T-7.5) positioned equidistant in a 3×3 matrix shape (Figure 12), which have an installed power of 5.5 kW. Flow straighteners and a honeycomb mesh are provided at the air inlet (Figure 11). The purpose of both elements is to break up the larger vortices, thus reducing the level of turbulence in the tunnel. The wind tunnel airspeed is controlled by a potentiometer that regulates the power output of the fans. The true airspeed is measured with a calibrated pitot tube and a pressure indicator *Druck DPI 150*.

Figure 11. Flow straighteners.

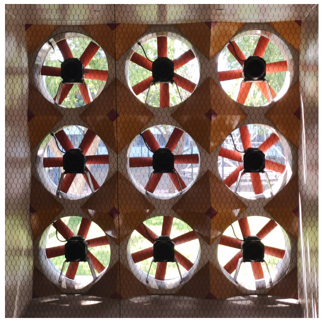

Figure 12. *N*ine fans HCT-90-4T-7.5.

In Figure 13, a diagram of the interconnection among the mentioned elements is presented, along with an image depicting the integration of the test stand into the wind tunnel (Figure 14).

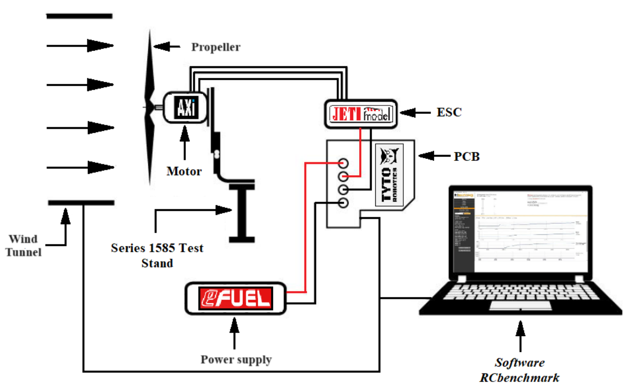

Figure 13. Setup diagram.

Figure 14. Setup integrated in wind tunnel.

THEORETICAL FRAMEWORK AND EXPERIMENTAL PROCEDURE

In this section, the theoretical framework of the project is described, encompassing propulsion fundamentals (Ref. 11). The methodology employed in the conducted test campaigns, both in static and dynamic conditions, this last one with the wind tunnel on, as well as the processing tools used, are discussed. The initial steps in static testing have proven indispensable for gaining confidence in handling the environment and detecting potential issues early on. Additionally, they yield initial results that drive the initiation of processing tool development. Therefore, in conjunction with the selection of the testing methodology, other aspects related to the encountered problems are examined.

Propulsion Theory

The characterization of an electric motor-propulsion system involves the measurement of the following parameters:

- Voltage - V (Volts).
- Current - I (Amps).
- Motor rotational speed - Ω (RPM).
- Thrust - T (N).
- Torque - Q (N·m).
- Velocity - V_∞ (m/s).

Thrust and torque are essential for studying the performance of the propulsion system, while voltage and current characterize the energy consumed by the motor. From these data, the motor efficiency (η_M), propulsive efficiency (η_P), and overall efficiency (η_{MP}) are defined:

$$\eta_M = \frac{\text{Mechanical Power}}{\text{Electrical Power}} = \frac{Q \cdot \Omega}{I \cdot V} \tag{1}$$

$$\eta_P = \frac{\text{Propulsive Power}}{\text{Mechanical Power}} = \frac{T \cdot V_\infty}{Q \cdot \Omega} = \frac{C_T}{C_P} J \tag{2}$$

$$\eta_{MP} = \eta_M \cdot \eta_P \tag{3}$$

Additionally, the results of the dimensionless coefficients of thrust (C_T), torque (C_Q), and power (C_P) need to be considered. These coefficients conveniently present the obtained results.

$$C_T = \frac{T}{\rho (nD)^2 D^2} = C_T\ (J,\ Re,\ M,\ geometry) \tag{4}$$

$$C_Q = \frac{Q}{\rho (nD)^2 D^3} = C_Q\ (J,\ Re,\ M,\ geometry) \tag{5}$$

$$C_P = \frac{P}{\rho(nD)^3 D^2} = C_P\ (J,\ Re,\ M,\ geometry) \quad (6)$$

Where nD and D^2 are taken as the velocity and reference surface, respectively. Dimensional analysis determines that the coefficients depend on the advance ratio J, Reynolds number, Mach number, and the geometry of the propeller. This dependence will be analyzed in detail in the following sections. In particular, the effects of Reynolds and Mach make the comparison of the coefficients not completely rigorous. The advance ratio is defined as:

$$J = \frac{V_\infty}{nD}, \quad (7)$$

and encompasses the different operating regimes of a propeller. Because J depends on both flow velocity and rotational speed, it acts analogously to the angle of attack (α) in aerodynamic lift calculations, determining how the blades interact with the incoming airflow and influencing C_T and C_P in a similar way. Different combinations of V_∞ and RPM modify the angle of attack of the blade profiles, distinguishing three operating regimes:

1. **Thrust-generating regime ($0 < J < J_1$):** positive thrust.
2. **Braking regime ($J_1 < J < J_2$):** negative thrust but requires power to produce it.
3. **Windmill or auto-rotation regime ($J > J_2$):** the propeller receives power from the air. This can be dangerous for two reasons: it can compromise the power supply infrastructure if it does not support negative currents, and control of the propeller rotation is lost, potentially exceeding its operating limit.

Data Processing

One of the crucial phases in achieving accurate results is conducting proper data processing. This processing was carried out using the Python programming language, which is currently expanding its presence in the industry due to its high potential in handling and analyzing vast amounts of information, especially in the realms of Data Analytics and Machine Learning techniques.

After each experiment, a `.csv` file is generated by the test stand, along with a `.txt` with additional information related to the wind tunnel airflow. To produce accurate and reliable results, an effective data processing method is crucial. The method encompasses data loading, filtering, interpolation, and representation, tailored to specific objectives (Figure 15). Data loading is performed using the `read_csv` function from `pandas` package, extracting the main variables (Thrust, Torque, Voltage and Current). Once loaded, the data undergoes an outlier detection step using the `EllipticEnvelope` function from the `scikit-learn` Python library. The 10% of data points that deviate furthest from the statistical center are removed. This filtering enhances robustness before interpolation. Subsequently, interpolation of the filtered main variables is carried out to generate continuous curves, from which the remaining parameters are defined, resulting in the final outcomes.

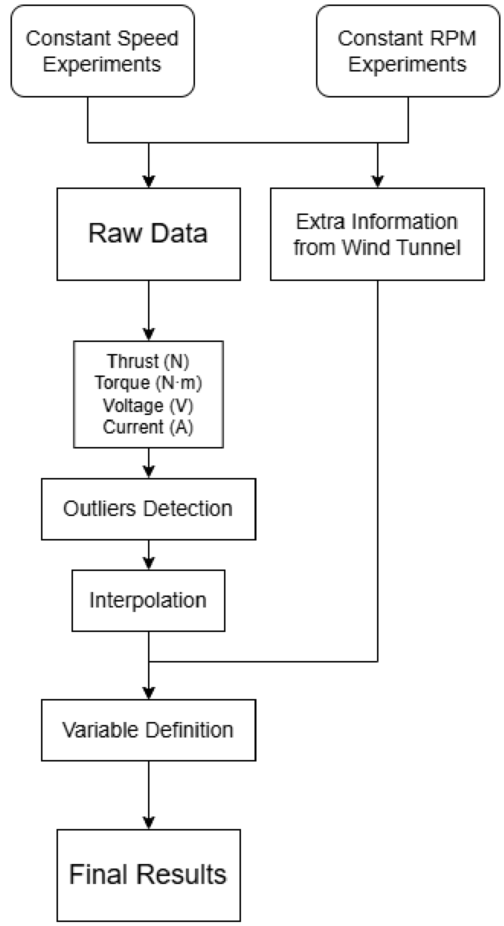

Figure 15. Data processing method.

Experimental Procedure

Before proceeding with the integration of the setup in the wind tunnel, a series of static tests were conducted to obtain preliminary results. The primary objectives of this campaign were to compare continuous and discrete data acquisition methods, determine the maximum achievable RPM for each motor and propeller combination, and explore the relationship between the PWM signal sent to the ESC and the motor RPM. The static tests were carried out using a nomenclature format of [Propeller Diameter]x[Pitch]_[Motor]_[Test Type].

There are two main approaches for acquiring data: the discrete sweep method, in which the RPM range is divided into steps, and the continuous sweep, where data is gathered in real-time across the entire RPM range. The efficiency of a system is most meaningful when it is in equilibrium, meaning the motor is running at a stable, constant RPM. In theory, the discrete sweep is ideal for this, as it allows time for the system to stabilize between each RPM step. However, another option is performing a continuous sweep with a low ramp rate, enabling the system to remain in near-continuous equilibrium throughout the test. In the investigation of this aspect, tests have been conducted both in discrete and continuous sweeps at different ramp rates. The comparison of results is carried out for configurations using the AXI 2826/10 V1 motor with three propellers: 13x4E, 13x10E, and 14x10E, along with configurations using the AXI 4130/16 and Aerodrive SK3 5045 motors with the 14x10E propeller. The identification of the different sweep tests in terms of rise time follows: *fast* (10 sec), *medium* (20 sec), *slow* (40 sec), *superslow* (60 sec) and *megaslow* (80 sec). Discrete sweep tests are referred to as *step*.

The raw results from experiments with the 13x4_2826 combination indicate that, while thrust barely varies between different types of tests, significant differences exist in key variables for calculating motor efficiency. The "fast" mode shows noticeable discrepancies in torque and mechanical power (Figures 16, 17), as the system fails to reach equilibrium before receiving new information. Nevertheless, the "megaslow" mode appears consistent for all variables and generally aligns with the trend of the discrete sweep test.

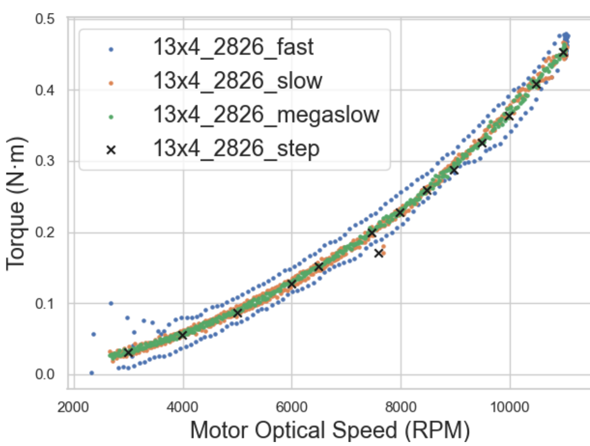

Figure 16. 13x4_2826: Torque ($N \cdot m$) vs RPM.

However, analyzing the curves of motor efficiency for the three tested propellers reveals that the "megaslow" results with the AXI 2826 motor are not as precise as expected, especially for high-pitch propellers (Figure 18). Cumulative discrepancies in variables lead to appreciable errors in efficiency. For larger motors like the AXI 4130 and Aerodrive SK3 5045, the interpolated curves from the continuous sweep tests seem to align well with the points from the discrete sweep tests (Figure 19). It is concluded that conducting tests in "megaslow" mode is feasible for larger motors, while smaller motors, especially with high-load propellers, struggle to reach equilibrium. Thus the discrete sweep method is elected as the most reliable approach, providing stable and consistent results across all combinations of motors and propellers.

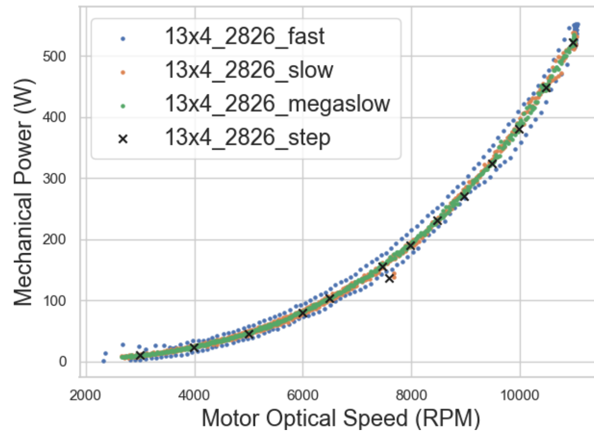

Figure 17. 13x4_2826: Mechanical Power (W) vs RPM.

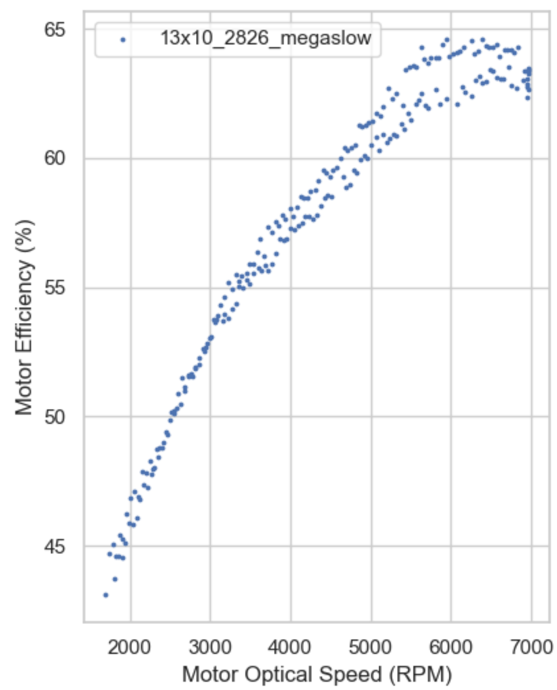

Figure 18. 13x10_2826: η_M (%) vs RPM.

In addition, the static testing campaign was crucial to understand the communication between the RCbenchmark software and the motors/ESC. By adopting the discrete sweep test methodology, the goal is to establish the relationship between the PWM pulse signal sent to the ESC and the motor RPM for each configuration. Using linear regression, it is determined that there is a common linear relationship between RPM and PWM signal for all motor and propeller combinations. This finding enables the automation of tests at specific RPM, incorporating the linear relationship into the codes as $PWM = 0,0577 \cdot RPM + 997$ (Figure 20).

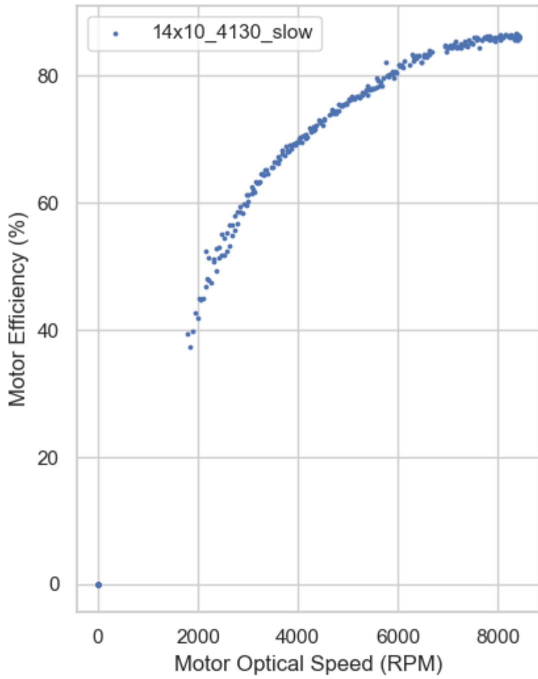

Figure 19. 14x10_4130: η_M (%) vs RPM.

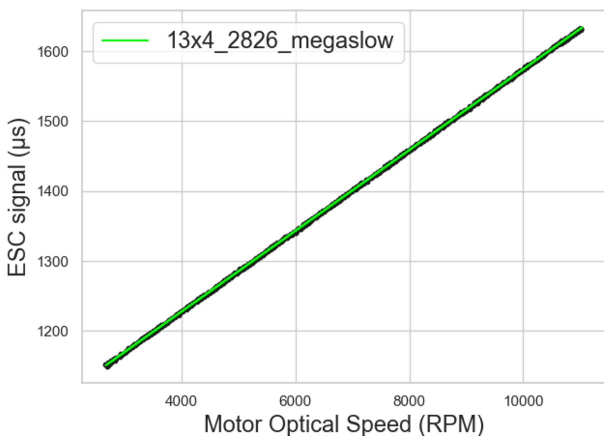

Figure 20. $PWM - RPM$ correlation.

During the wind tunnel test campaign, a 3x5 combination matrix is established for testing, covering every propeller (13x4E, 13x10E, 14x10E) and motor (AXI 2826/10, AXI 2826/10 V2, AXI 4130/16, AXI 4130/16 V2, SK3 5045). With the introduction of flow speed as a new variable, two types of experiments are conducted: constant speed and constant RPM tests. It is important to highlight that although both types of experiments were carried out for comparison purposes, only one of them would be sufficient to generate valid results.

In constant speed tests, several experiments are performed from the tunnel turned off to a progressive 10% to 80% ($\approx$ 80 km/h) increase in tunnel speed. It is emphasized that, with the speed increase, the propeller could enter auto-rotation, not of interest to this project. Therefore, the minimum RPM value is adjusted based on the tunnel percentage, avoiding the inclusion of irrelevant data and maintaining a total of 15 steps within the area of interest. Nomenclature: [Propeller Diameter]x[Pitch]_[Motor]_[Speed %]_[Test Type].

Constant RPM tests involve fixing the motor's angular velocity and conducting a sweep in tunnel speed. This type of experiment is carried out manually, taking approximately 100 entries for each speed step. Subsequently, in the data processing, 50 valid entries are selected for each step. RPM jumps are made every 1000 RPM, adhering to the safety cutoff restrictions of each motor. Nomenclature: [Propeller Diameter]x[Pitch]_[Motor]_[RPM]_[Test Type].

The two types of experiments are compared, initially focusing on the combination 14x10_2826v2 and extending the conclusions to the rest. Upon examining Figure 21, it becomes evident that the results from constant speed experiments yield more data points to recreate the curves, achieving a more effective smoothing. This issue becomes more pronounced as the tunnel percentage increases. Additionally, the second method, which involves RPM jumps in multiples of 1000, typically does not cover the region near auto-rotation or reach maximum revolutions, unlike the first method, which adjusts to both limits in each trial. For these reasons, constant speed experiments appear to be the more suitable approach.

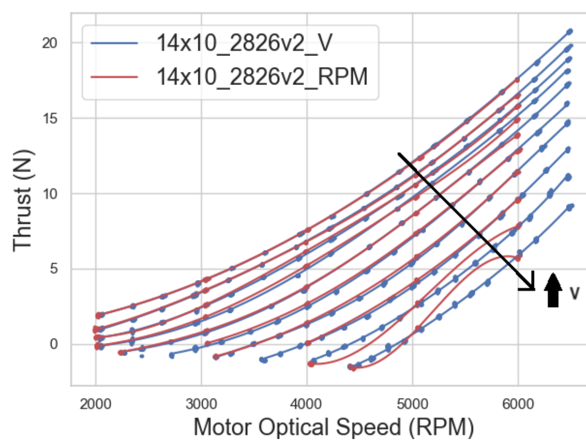

Figure 21. Test type comparison.

In summary, the discrete sweep method, combined with constant speed experiments in the wind tunnel, has been selected as the standard methodology for the subsequent result analysis. This approach ensures accurate and reproducible results across all motor and propeller combinations, while also providing improved curve smoothing for key variables and a more comprehensive representation in areas of maximum RPM and auto-rotation, particularly at higher wind tunnel speed percentages.

The concept of equilibrium has been discussed, referring to the state when the motor is running at a stable, constant RPM. Although time was allowed for the setup to stabilize at each step, it is necessary to validate that this equilibrium is indeed reached before collecting data. This is why a statistical validation was carried out to ensure the stability of the setup during the experiments.

For the validation of equilibrium, thrust data points were analyzed. This analysis is shown for the 13x4_5045 combination, although similar results were observed for the other combinations. At each step or ESC signal setting, the thrust values were collected, and both the mean and variance of the data were computed, revealing low variation as shown in Figure 22. Additionally, box plots were generated to visualize the distribution of the thrust and examine potential outliers. The box plots in Figure 23 clearly demonstrate the low variation in thrust values, with the majority of data points concentrated around the median, indicating consistent performance of the system. The minimal spread of data points and the absence of significant outliers further validate that the system remained in equilibrium during the tests.

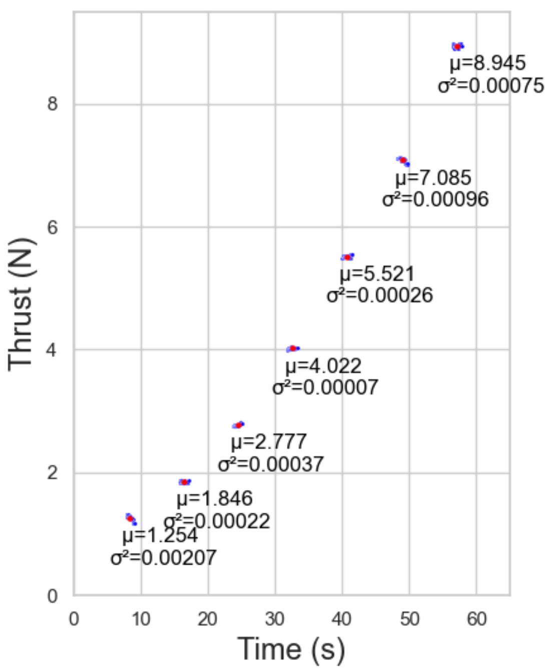

Figure 22. Thrust mean and covariance.

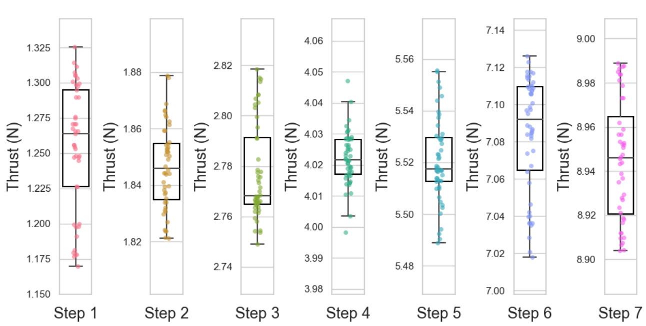

Figure 23. Thrust box plots for each step.

ANALYSIS AND COMPARISON OF RESULTS

The amount of information gathered from the wind tunnel test campaign is extensive, and it is crucial to organize it effectively for analysis. Initially, a comparison between AXI motor versions will be conducted, followed by a comprehensive analysis of all generated content. For brevity, graphs are only presented for the 14x10_4130v2 configuration; however, the insights extend to other configurations, for which maximum efficiency values are reported. After drawing conclusions from the analysis, the comparison of performances among different motor and propeller combinations will be carried out for each operating regime.

AXI Motors Discussion

In this section, the efficiency results for the AXI 2826/10 and AXI 4130/16 motors, both in their old and new versions, are compared. This comparison is conducted at idle (1%) tunnel speed, aiming to achieve two objectives:

1. Verify the claimed improvement in efficiency by the manufacturer.
2. Prove that the obtained results follow the same trend, allowing the exclusion of the old motors from the final results section, as the difference with the new version does not go beyond a slight enhancement in efficiency.

In Figures 24, 25, a significant improvement in the efficiency of both motors is evident, attributed to the reduction of internal resistance and enhancements in cooling. The performance increase is observed in cases with the tunnel at idle (1%) for each propeller, with those meeting the manufacturer's specified improvements highlighted in green (2% for 2826/10 and 1% for 4130/16) (Tables 2, 3). Efficiency improves notably with low-pitched propellers, although this improvement tends to decrease when increasing tunnel speed. However, the announced maximum efficiency values (86% and 89%) are not achieved in any case.

Table 2. AXI 2826: η_M^{max} at idle speed (1%).

Propeller	V1 (%)	V2 (%)	Improvement (%)
13x4E	73.98	76.70	**2.72**
13x10E	63.31	64.74	**1.43**
14x10E	63.65	65.28	**1.63**

Table 3. AXI 4130: η_M^{max} at idle speed (1%).

Propeller	V1 (%)	V2 (%)	Improvement (%)
13x4E	84.19	86.16	**1.97**
13x10E	84.46	85.49	**1.03**
14x10E	85.09	85.83	**0.74**

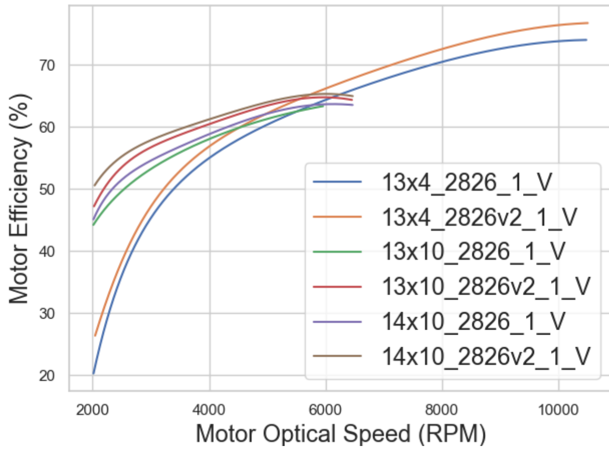

Figure 24. AXI 2826: η_M (%) vs RPM - Version Comparison.

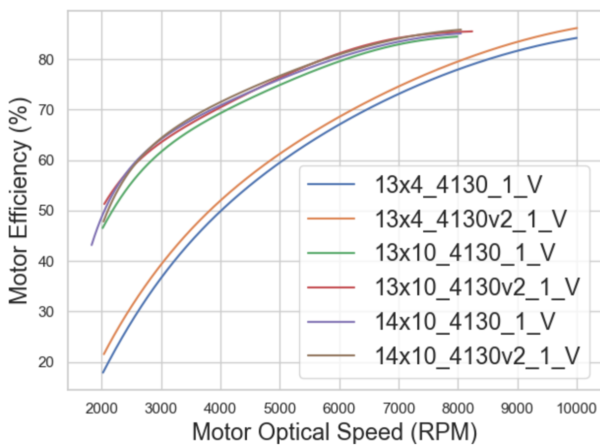

Figure 25. AXI 4130: η_M (%) vs RPM - Version Comparison.

In conclusion, the performance increase in AXI motors is confirmed, but the overall trend remains consistent. Therefore, for the final results, only the improved V2 versions will be considered and compared, along with the Turnigy motor.

Analysis of Main Variables: T, Q, I, V

Observing Figure 26, it is noticeable that thrust increases with revolutions but decreases as the flow speed increases. Furthermore, for both the thrust (Figure 26) and torque (Figure 27), it can be observed that at low RPM, the values are below 0. This is the range where the propeller slightly enters a braking regime, generating negative thrust but demanding power, eventually entering auto-rotation. The auto-rotation range is entirely defined in Figure 28, where the current takes negative values. Subtle changes in voltage are observed, as a result of the use of a continuous power supply (Figure 29).

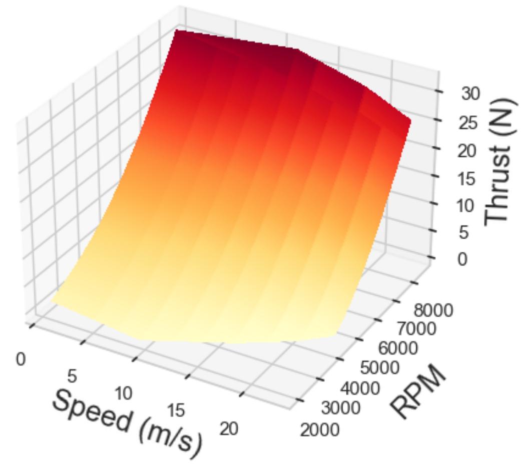

Figure 26. Thrust (N) vs RPM vs Speed (m/s).

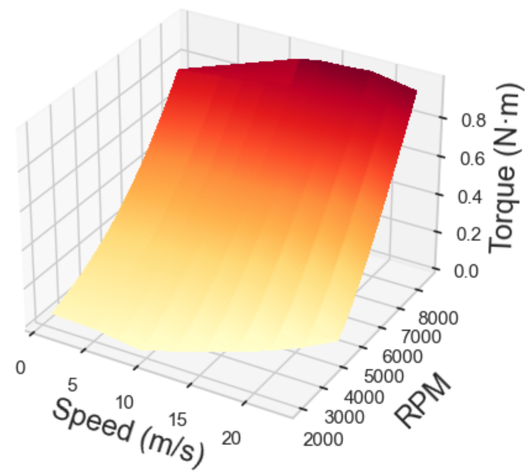

Figure 27. Torque ($N \cdot m$) vs RPM vs Speed (m/s).

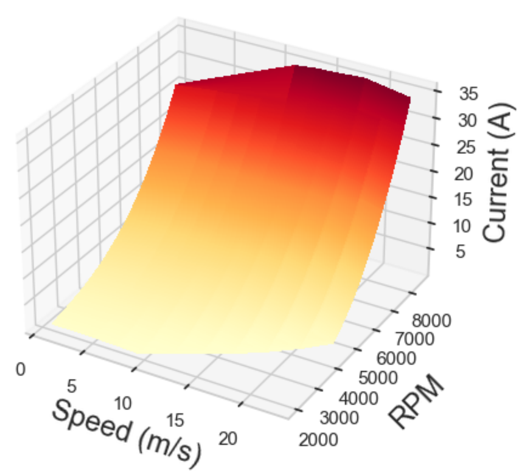

Figure 28. Current (A) vs RPM vs Speed (m/s).

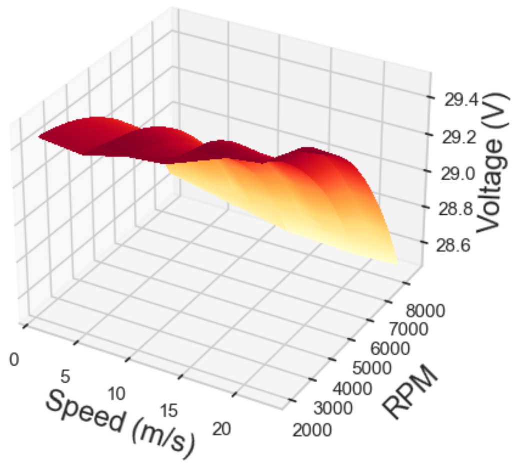

Figure 29. Voltage (V) vs RPM vs Speed (m/s).

Analysis of Dimensionless Coefficients: C_T, C_P

The advance ratio parameter, J, defined in Equation 7, is capable of encompassing the different operating regimes of a propeller in a vector by combining flow velocities and motor revolutions. Before delving into that, it is advisable to analyze the effects of compressibility that arise at the blade tip at high Mach numbers. This effect becomes significant when the propeller operates at high revolutions, particularly noticeable beyond $M = 0,3$. The correction for these effects is carried out using the Prandtl-Glauert analogy, established to relate the profile pressure coefficient and wing lift coefficient for $M > 0,3$ to those calculated for incompressible flow. In general, the lift coefficient of a wing is defined as:

$$C_L = \frac{C_L^i}{\sqrt{1 - M_\infty^2}} \tag{8}$$

Where C_L is the actual lift coefficient and C_L^i is the one obtained for incompressible flow. The correction applies similarly to the geometry. This idea can be extrapolated to a rotating wing (propeller) with a diameter D, assuming a relationship between dimensionless coefficients for both regimes (Ref. 12):

$$C_T = \frac{C_T^i(D^i)}{\sqrt{1 - M_\infty^2}}, \qquad C_P = \frac{C_P^i(D^i)}{\sqrt{1 - M_\infty^2}} \tag{9}$$

$$D = \frac{D^i}{\sqrt{1 - M_\infty^2}} \tag{10}$$

Where Mach is determined by the vectorial result of tangential and transverse air velocities at 75% of the root on the blade. Therefore:

$$M_\infty = \frac{\sqrt{\left(\frac{3}{4}\frac{D}{2}\Omega\right)^2 + V_\infty^2}}{\sqrt{\gamma R_g T}} \tag{11}$$

Here, Ω is the rotational speed of the propeller, V_∞ is the flow velocity, and $\sqrt{\gamma R_g T}$ is the speed of sound under corresponding conditions. Starting from the definition of Coefficients 4 and 6:

$$C_T = \frac{\frac{T^i}{\rho_\infty n^2 (D^i)^4}}{\sqrt{1 - M_\infty^2}} = \frac{\frac{T^i}{\rho_\infty n^2 D^4 (1-M_\infty^2)^2}}{\sqrt{1 - M_\infty^2}} = \frac{\frac{T^i}{\rho_\infty n^2 D^4}}{(1 - M_\infty^2)^{\frac{5}{2}}} = \frac{C_T^i(D)}{(1 - M_\infty^2)^{\frac{5}{2}}} \tag{12}$$

$$C_P = \frac{\frac{P^i}{\rho_\infty n^3 (D^i)^5}}{\sqrt{1 - M_\infty^2}} = \frac{\frac{P^i}{\rho_\infty n^3 D^5 (1-M_\infty^2)^{\frac{5}{2}}}}{\sqrt{1 - M_\infty^2}} = \frac{\frac{P^i}{\rho_\infty n^3 D^5}}{(1 - M_\infty^2)^3} = \frac{C_P^i(D)}{(1 - M_\infty^2)^3} \tag{13}$$

Moreover, since the advance ratio parameter depends on the geometry, it must also be corrected:

$$J = J^i \sqrt{1 - M_\infty^2} \tag{14}$$

Applying compressibility corrections consolidates the coefficient curves across experiments, improving coherence and enabling better cross-configuration comparisons.

As seen in Figures 30 and 31, the values of C_T increase as the revolutions increase, that is, with the decrease of J. Similarly, an increase in revolutions also implies the demand for more electrical power (or current for the continuous power supply); hence, the trend of C_P is also to increase when J decreases.

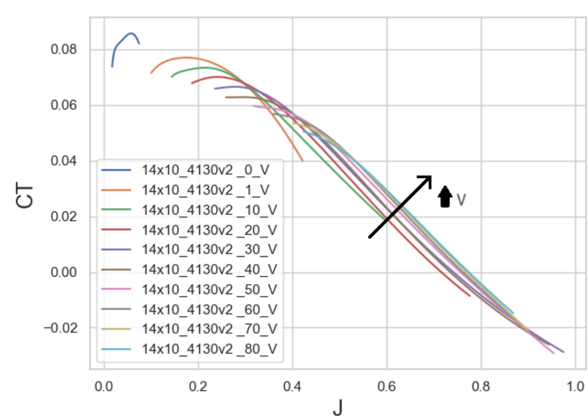

Figure 30. C_T vs J with compressibility effects.

It is also noticeable how the consideration of compressibility effects (Figures 30, 31) implies a reduction in the maximum values of C_T and C_P for all experiments, and the different curves appear to cluster following a common trend, as opposed to Figures 32, 33.

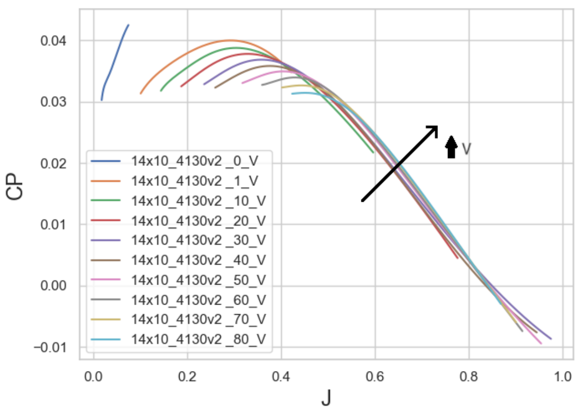

Figure 31. C_P **vs** J **with compressibility effects.**

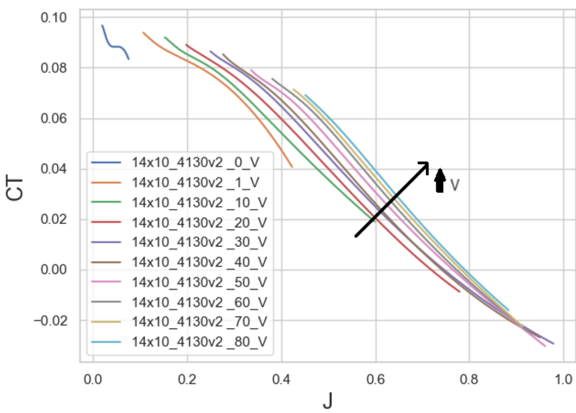

Figure 32. C_T **vs** J **without compressibility effects.**

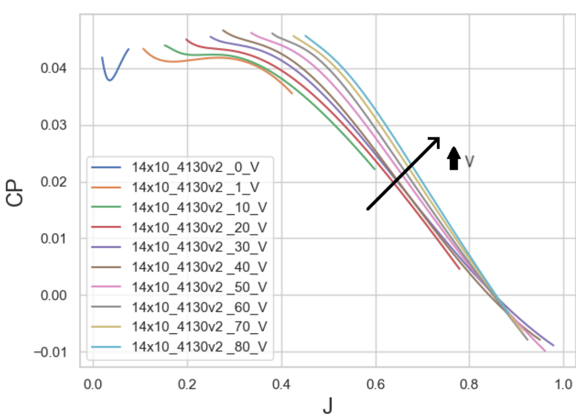

Figure 33. C_P **vs** J **without compressibility effects.**

Analysis of Efficiencies: η_M**,** η_P**,** η_{MP}

The motor efficiency, η_M, increases with the flow velocity, but the primary contribution comes from the increase in revolutions (Figure 34). In relation to J, the efficiency improves as J decreases. The transition to maximum efficiency is accentuated with an increase in speed.

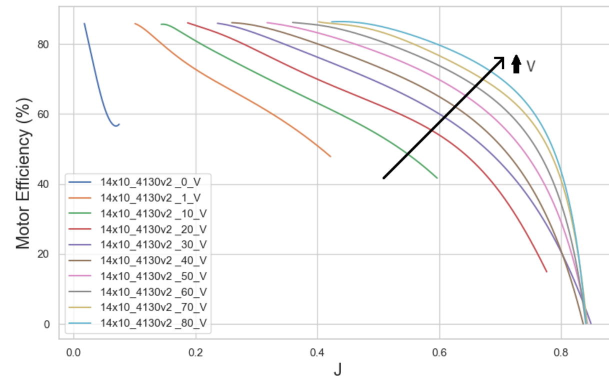

Figure 34. η_M **(%) vs** J **with compressibility effects.**

As can be noticed in Table 4, the motor is designed to be efficient when it spins faster, thus maximum efficiency is reached for maximum RPMs, constrained by operational limits for each combination.

Table 4. Maximum values of motor efficiency, η_M^{max}**.**

Propeller	Motor	η_M^{max} (%)	Ω (RPM)	V_∞ (m/s)
13x4	2826v2	78.3	10540	19.9
	4130v2	86.8	10000	7.4
	5045	84.5	10520	9.24
13x10	2826v2	66.9	6040	22.8
	4130v2	86.4	8240	22.6
	5045	81.7	7320	22.2
14x10	2826v2	68.7	6490	22.6
	4130v2	86.4	8240	22.7
	5045	82.8	7780	22.8

Regarding propeller efficiency, η_P, it is inferred that the propeller is more efficient the higher the incident velocity, with an optimal range of RPM where performance is maximum. The combination of V_∞ and RPM is directly involved in the angle of attack seen by the blade profile. Therefore, designed with an α_{opt}, an increase in V_∞ unquestionably implies an increase in RPM to maintain the optimum point. This is observed in Figure 35, where the optimal RPM value grows as the velocity increases, emphasizing that the propeller is optimal for a specific design point. Later, when comparing propellers of different pitches, this effect will be better appreciated.

After this clarification, one might question why efficiency increases with velocity. It is crucial not to make the mistake of generalizing all the graphs from the 10 experiments into one. The same value of the advance ratio can be achieved by different combinations of velocity and revolutions, each associated with a different Reynolds number. In the previous figures, it is understood how efficiency improves with an increase in Reynolds number, also expanding the operating range of the propeller. For this reason, the comparison of coefficients and performances does not become entirely rigorous. Additionally, it opens the door to studying performance as a function

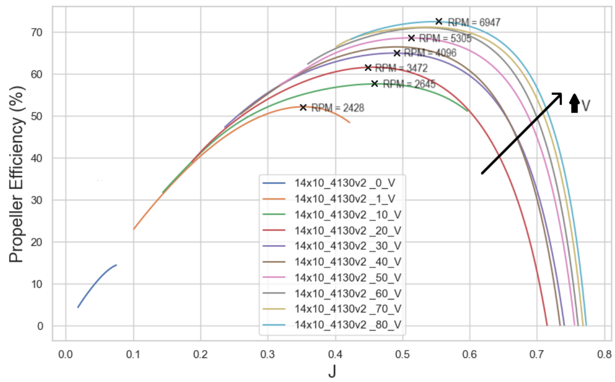

Figure 35. η_P **(%) vs** J **with compressibility effects.**

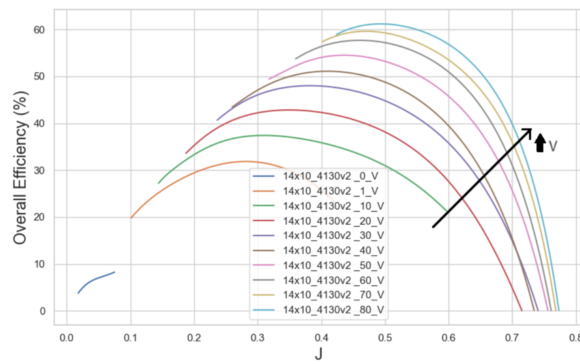

Figure 36. η_{MP} **(%) vs** J **with compressibility effects.**

of operating altitude, which would also affect Reynolds number but falls outside the scope of the project.

The maximum values for each combination are presented in Table 5. As stated before, although propellers generally become more efficient at higher speeds, the low-pitch propeller reaches its maximum values at lower speeds. This occurs because the increase in flow speed cannot be sufficiently offset by increasing RPM to maintain optimal performance.

Table 5. Maximum values of propeller efficiency, η_P^{max}**.**

Propeller	Motor	η_P^{max} (%)	Ω (RPM)	V_∞ (m/s)
	2826v2	57.3	10500	17.7
13x4	4130v2	53.0	10020	18.3
	5045	56.8	10540	17.7
	2826v2	77.0	5900	22.8
13x10	4130v2	76.6	5420	22.6
	5045	80.8	5230	22.2
	2826v2	73.6	6490	22.6
14x10	4130v2	72.4	6740	22.7
	5045	72.7	6870	22.8

Finally, the overall efficiency, η_{MP}, bears a strong resemblance to the propeller efficiency, becoming its increase with flight speed more noticeable (Figure 36). There is also a strong correlation between the speed and RPM values at which both maximum propeller and overall efficiency are achieved (Table 6).

The comprehensive understanding of different flight regimes involves plotting C_T, C_P, and η_P values in a single graph for fixed Re and V_∞. Due to experimental constraints, such as maximum RPM recommended by the manufacturer and power source limits, a complete curve with a single speed percentage is impractical. For this reason, all curves of C_T, C_P and η_P shown in Figure 37 are interpolated into the results of Figure 38. This supports qualitative comparison across operating regimes, curves and allows identification of transitions between thrust-generating, braking and auto-rotation regimes across configurations.

Increasing the advance ratio J raises the effective pitch angle, which reduces the angle of attack, thrust, and power. At

Table 6. Maximum values of overall efficiency, η_{MP}^{max}**.**

Propeller	Motor	η_{MP}^{max} (%)	Ω (RPM)	V_∞ (m/s)
	2826v2	44.9	10500	17.7
13x4	4130v2	45.1	10000	15.9
	5045	47.6	10540	17.7
	2826v2	51.4	5950	22.8
13x10	4130v2	61.2	6295	22.6
	5045	61.1	6070	22.2
	2826v2	50.6	6490	22.6
14x10	4130v2	61.2	7400	22.7
	5045	59.7	7300	22.8

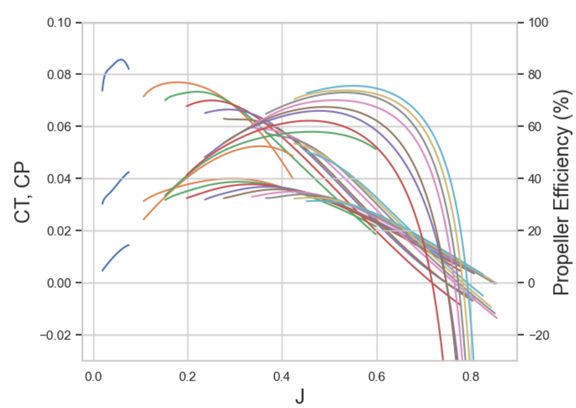

Figure 37. C_T, C_P, η_P **(%) vs J.**

a specific point J_1, where the thrust coefficient $C_T = 0$, the propeller produces no thrust but still requires torque to overcome viscous forces—keeping the power coefficient C_P positive. This marks the beginning of the braking regime, in which the propeller generates negative thrust while still consuming power. Between J_1 and J_2 (where $C_P = 0$), the propeller continues in this braking mode. At J_2, the system transitions into auto-rotation, where power is extracted from the flow, potentially reversing current direction, which can pose safety risks.

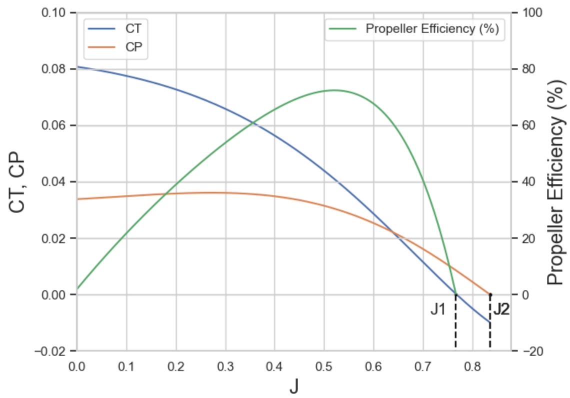

Figure 38. C_T, C_P, η_P (%) **vs J, interpolated.**

Comparison of Efficiencies: η_M, η_P, η_{MP}

The comparison of motor efficiency between configurations is carried out through constant Mach curves, as interpolation between curves from different experiments is not feasible due to significant data dispersion. Among the tested conditions, $M = 0,15$ was the only value for which all motor–propeller combinations provided a complete and overlapping dataset, allowing for direct and meaningful comparison.

In Figure 39, it can be seen that the small motor, AXI 2826/10, is the best option when choosing a low-pitch propeller. Additionally, its maximum in efficiency remains the same for high-pitch propellers. When comparing between large motors, the AXI 4130/10 outperforms the SK3 5045 across almost the entire operating range.

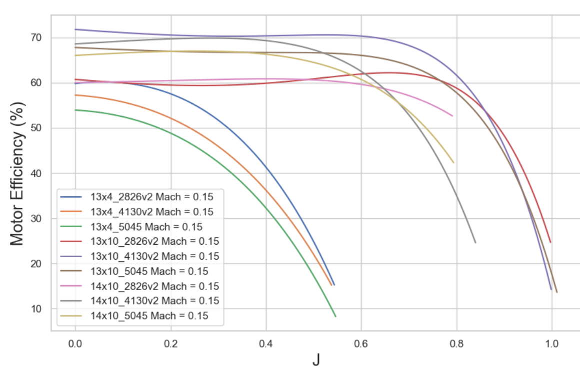

Figure 39. η_M (%) **comparison at** $M = 0,15$.

Finally, it can be deduced that it is always more advantageous to select higher-pitch propellers in terms of motor efficiency. Generally, they broaden the motors operating range, and efficiency improves significantly for the larger ones.

Regarding propeller efficiency, it is first interesting to analyze the impact of pitch on the propeller's performance. The angle of the incident flow depends on both the rotation and flight speed. This angle increases as J does, simultaneously decreasing the angle of attack of the airfoil, that may reach negative values, entering into air-braking regime.

Therefore, it is well-known and observable that flying at top speeds implies the need to use propellers with a higher pitch, offering greater maximums. On the other hand, in a low-speed regime, a high pitch implies an excessively high angle of attack, leading to stalling and resulting in low efficiency values; whereas a low-pitch propeller could fly with α_{opt}. The issue with low-pitch propellers is that the operating range is significantly reduced. For a high-pitch propeller, the range is broader, even though it is less efficient at low speeds. To optimize efficiency across the full flight envelope, the use of variable-pitch propellers is recommended. These can dynamically adjust blade pitch to maintain the optimal angle of attack as flight speed and RPM vary, ensuring high efficiency in both low- and high-speed regimes.

In terms of diameter, it can be observed that a greater diameter result in a decrease in both the maximum propeller efficiency and its operating range. Finally, it is noticeable how the propeller's performance is independent of the mounted motor (Figure 40).

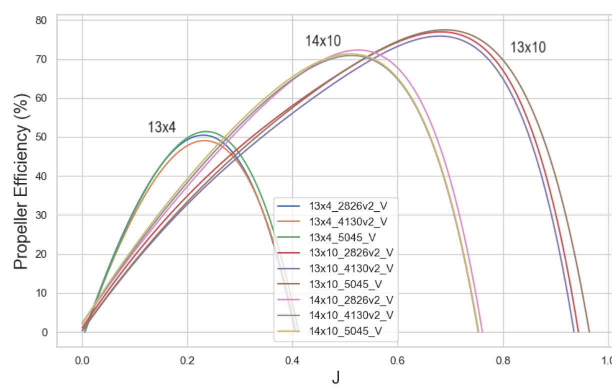

Figure 40. η_P (%) **comparison, interpolated.**

Finally, the combination of the previous curves result in the overall efficiency of the system, that brings together the insights gained earlier. The concluding graph of the analysis is presented in Figure 41, which consolidates every experiment carried out, and from where one can point out the best motor-propeller configuration for each operating regime.

PRACTICAL APPLICATION

The experimental data and motor efficiency models developed in this study are currently being integrated into the performance simulator for the ProVANT-EMERGENTIa UAV platform. This integration enables high-fidelity simulations of propulsion behavior across a range of mission profiles, thus supporting informed design decisions such as motor–propeller matching, battery sizing, and endurance estimation for SAR operations. A preliminary application of this model can be found in the single-segment performance analysis presented in (Ref. 13), where it was used to optimize a tilt-rotor RPAS configuration.

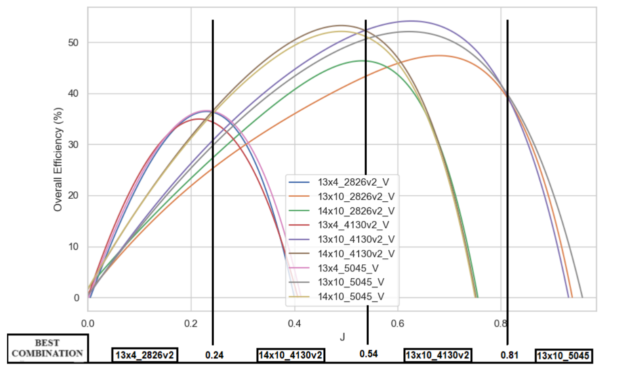

Figure 41. η_{MP} **(%) comparison, interpolated.**

CONCLUSION

This article has presented the wind tunnel experiments conducted on the candidate propulsive system of a small electric aircraft, with the objective of creating a robust testing and data processing methodology. One of the main contributions has been the optimization of the testing procedure, relying on the integration of a commercial test stand. With the introduction of a continuous power supply, dependence on charge cycle has been eliminated, being the setup continuously available for testing. It is concluded that the most effective way to characterize the propulsion system across its entire operating range is through experiments at constant speed, adjusting the RPM sweep range accordingly. Additionally, effective integration of the setup in the wind tunnel and improvements in the processing methodology have been achieved.

Regarding the analysis of tested configurations, it has been verified that the new versions of the AXI motors show an improvement in efficiency of approximately 2-4%. It has been noted that motor performance is mainly dependent on RPM, and the significant influence of pitch and diameter on propeller performance. Finally, it is possible to determine, among the tested combinations, the most suitable for each flight regime.

Future project lines derived from this work are: the realization of further wind tunnel experiments addressing new motor-propeller combinations, variable-pitch propellers, the introduction of new parameters such as incidence angle, and the study of wing-propeller and propeller-propeller interference. Moreover, efficiency losses introduced by the ESC should be considered. With a substantial number of new experiments, the groundwork is laid for the creation of accurate multivariable models. These models offer a deeper understanding of the interrelation of key parameters that have an influence on the system and serve as a basis to obtain precise and real information that can be incorporated into already developed simulators to model with high fidelity the performances of electric aircraft.

Author contact:
Mario Navarro-Zea: marionavarrozea@gmail.com
Sergio Esteban: sesteban@us.es.

ACKNOWLEDGMENTS

Acknowledgements to the AIRBUS Chair year 2024.

REFERENCES

1. Haro, S., and Esteban, S., "Parametric Aerodynamic Study of a Convertible Aircraft Using CFD Tools. ProVANT EMERGENTIa Project". *Synergetic Cooperation Between Robots and Humans: Proceedings of the CLAWAR 2023 Conference—Volume 1*. Lecture Notes in Networks and Systems, vol. 810, pages 141–151. Springer, 2024. DOI: 10.1007/978-3-031-47269-5_15.

2. Hattenberger, G., Drouin, A., Bronz, M., "Electric Propulsion System Characterization through Experiments". *University of Toulouse*, ENAC, Toulouse.

3. Deters, R.W., Ananda, G.K., Selig, M.S., "Reynolds Number Effects on the Performance of Small-Scale Propellers". 32nd AIAA Applied Aerodynamics Conference, Atlanta, GA, 2014. DOI: 10.2514/6.2014-2151.

4. Kutty, H.A., Rajendran, P., Mule, A., "Performance analysis of small scale UAV propeller with slotted design". 2nd International Conference for Convergence in Technology, I2CT 2017. DOI: 10.1109/I2CT.2017.8226219.

5. Jiménez, J.H., Hoyos, J.D., Echavarría, C., Alvarado, J.P., "Exhaustive Analysis on Aircraft Propeller Performance through a BEMT Tool". *Journal of Aeronautics, Astronautics and Aviation* 54, 13-24, 2022. DOI: 10.6125/JoAAA.202203_54(1).02.

6. Series 1585 Test Stand documentation, Tyto Robotics. Available: `https://www.tytorobotics.com/pages/series-1580-1585` [Accessed: 30-May-2025].

7. AXI Motors documentation, Model Motors. Available: `https://www.modelmotors.cz/about-axi/` [Accessed: 30-May-2025].

8. Mezon 115 Opto documentation, Jeti Model. Available: `https://www.jetimodel.com/katalog/mezon-115-opto.htm` [Accessed: 30-May-2025].

9. APC Propellers technical information, APC Propellers. Available: `https://www.apcprop.com/technical-information/?v=cd32106bcb6d` [Accessed: 30-May-2025].

10. eFuel 1200W documentation, SkyRC. Available: `https://www.skyrc.com/psu_50a?from=category` [Accessed: 30-May-2025].

11. Espín, A.F., Rivas, D.R., "Fundamentos de Propulsión". *Escuela Técnica Superior de Ingeniería*, Universidad de Sevilla, Sevilla.

12. Franco-Espín, A., Esteban, S., “Analogía de Prandtl-Glauert para alas giratorias”. *Escuela Técnica Superior de Ingeniería*, Universidad de Sevilla, Sevilla.

13. Martínez, A., Franco-Espín, A, and Esteban, S., “Single-Segment Analysis for the Performance Optimization of a Tilt-Rotor All-Electric RPAS. ProVANT-EMERGENTIa Project”. In *Synergetic Cooperation Between Robots and Humans: Proceedings of the CLAWAR 2023 Conference—Volume 1*. Lecture Notes in Networks and Systems, vol. 810, pp. 129–140. Springer, 2024. DOI: 10.1007/978-3-031-47269-5_14.